Hippocampal trace coding dominates and disrupts place coding

Hannah S Wirtshafter[1*], Mayank R Mehta[2], Sara A Solla[1], John F Disterhoft[1]

*Lead contact: hsw@northwestern.edu (HSW)

1. Department of Neuroscience, Northwestern University Feinberg School of Medicine, Chicago, IL, USA.

2. W. M. Keck Center for Neurophysics, Departments of: Physics & Astronomy, Neurobiology, Neurology, University of California, Los Angeles, Los Angeles, CA 90095, USA.

Abstract

The hippocampus is widely viewed as a spatial mapping system because many CA1 neurons show location-specific activity during exploration. However, the hippocampus is also required for non-spatial learning, including trace eye-blink conditioning. Because most prior reports of non-spatial signals were obtained in immobile animals, it has been proposed that the hippocampus encodes space during locomotion and non-spatial variables during immobility. To test this directly, we used calcium imaging to record thousands of CA1 neurons while rats performed trace eye-blink conditioning during free exploration of an open field. Across more than 6,000 neurons from five rats, mean firing rates during trace-conditioning periods were ~1.5-fold higher than during non-trial periods, and this difference persisted after controlling for locomotor speed. At the single-cell level, task-related modulation was widespread and strongly biased toward increased firing. Task-enhanced neurons outnumbered spatially selective neurons by more than threefold, indicating that trace coding predominated over place coding. Although trace-conditioning events occurred at random spatial locations and during continuous locomotion, trace-related activity remained robust at both single-cell and population levels. In contrast, spatial coding was reduced during trace periods, with lower spatial information and decreased similarity between task and non-task rate maps. These findings show that during active behavior, trace coding dominates and disrupts place coding, challenging the view that the hippocampus functions primarily as a stable spatial map.

Introduction

The hippocampus is widely regarded as a spatial mapping system because many CA1 neurons exhibit location-specific activity during exploration[1-8]. However, the hippocampus is also required for a range of non-spatial cognitive tasks[9-13] and exhibits task-related activity during these behaviors[14-28], including trace eyeblink conditioning (the 'trace task')[15,16,18,29-34]. Because most reports of non-spatial hippocampal signals were obtained in immobile or head-fixed animals[14,15,35,36], it has been proposed that spatial variables dominate during locomotion, whereas non-spatial variables are represented primarily during immobility[6,7,37,38]. Many studies of hippocampal involvement in non-spatial tasks similarly constrain movement or tightly couple task structure to spatial position[30,39], limiting the ability to dissociate spatial and non-spatial variables. Few studies have directly tested this idea, yielding mixed and sometimes conflicting results[12,37]. Whether non-spatial signals reflect genuine task encoding during active exploration rather than indirect modulation of spatial firing remains unresolved.

To address this question, we recorded large populations of CA1 neurons using calcium imaging while rats performed trace eyeblink conditioning during free exploration of an open field. This experimental design allowed us to dissociate spatial position, movement, and task structure while monitoring hippocampal activity at both the single-cell and population levels.

56
57 **Results**
58 We trained a cohort of five freely moving rats on the trace task while recording neural activity from the
59 dorsal CA1 region using miniature microscopes and the calcium indicator GCaMP8m. In this task, each
60 trial consists of a 250ms auditory tone (conditioned stimulus, CS), followed by a 500 ms trace interval
61 with no stimuli, and then a 100ms eyelid shock (unconditioned stimulus, US) (Fig. 1a-b). Inter-trial
62 intervals were randomly varied between 30 and 60 seconds (mean 45s). Blink responses and shock
63 delivery were monitored using EMG wires implanted in the eyelid muscle (see Methods). Throughout
64 training and testing, animals were allowed to move freely within the behavioral arena (78.7cmx50.8cm
65 box), and they did not exhibit freezing or pausing during trials (Fig. 1c). Data were analyzed only in those
66 sessions where the rats performed the trace task on at least 70% of trials across three consecutive
67 sessions (See Methods, Fig. S1).
68
69 We recorded and analyzed a total of 6192 dorsal CA1 cells from five rats across 15 sessions, three
70 sessions per rat (See Methods). Many neurons showed clear spatial modulation, consistent with
71 extensive literature on place cells[4,40,41](Fig. 1d,e, upper-left panels, S2). Simultaneously, recorded
72 neurons also showed distinct responses during different phases of the task, with their activity aligned to
73 either the tone, trace interval, eyelid shock, or post-shock period, and these responses were quite stable
74 across trials (Fig. 1d-e, S2). The rats were at diverse locations throughout the maze during these trials,
75 yet the neurons were active selectively and reliably during specific epochs of the trace task, showing
76 that the trace-responses were not merely spatial responses. In fact, neural activity during the trace task
77 was so reliable that the neuron's spatial selectivity was substantially degraded and differed compared to
78 the non-task periods. We did several analyses and controls to test these observations, as follows.
79

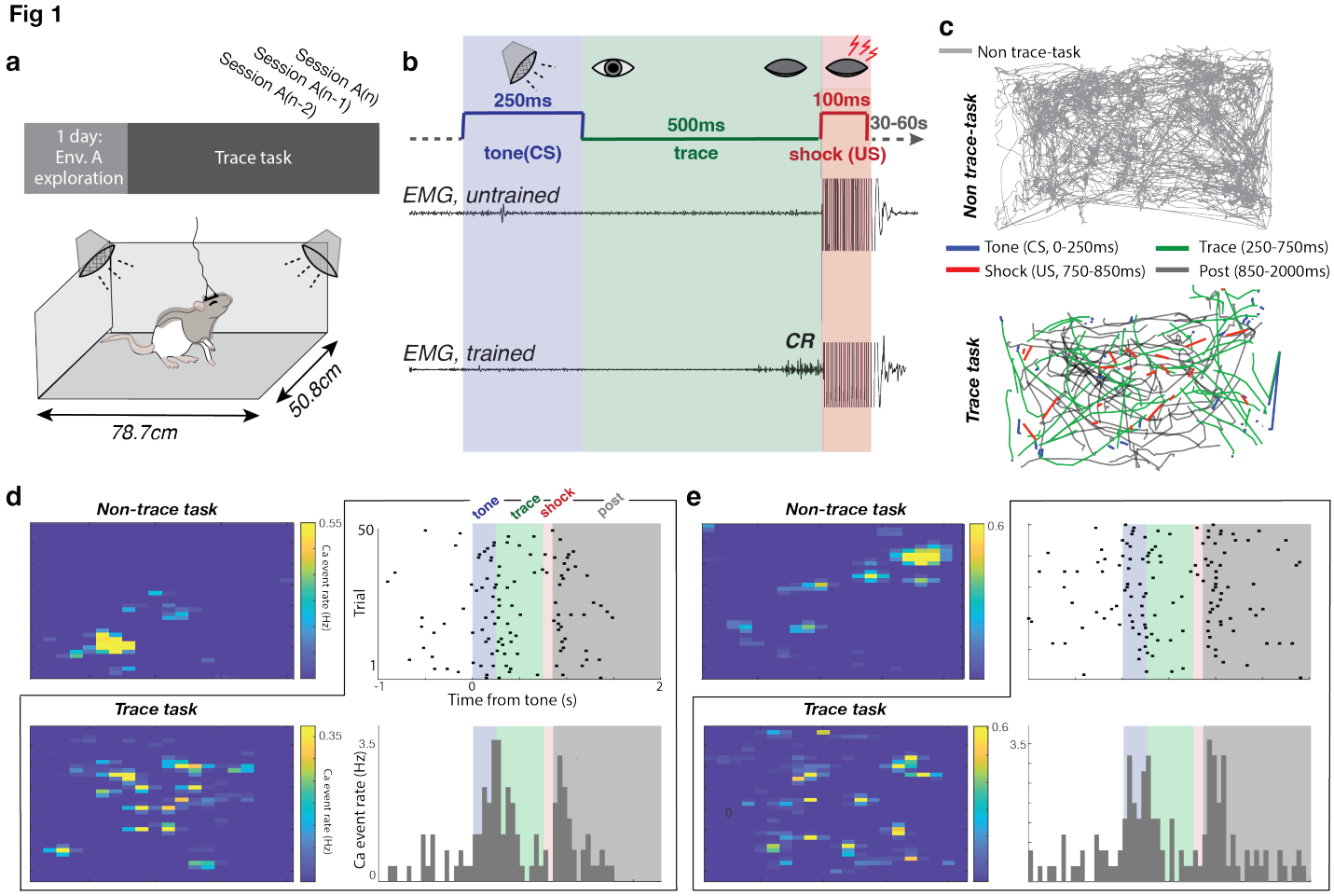

Figure 1. Schematic of task and cell responses

a. Schematic of the trace eyeblink conditioning (trace task) environment. After one day of exploration in the conditioning environment, rats were trained daily in the trace task until reaching behavioral criterion

b. Schematic of the trace eyeblink conditioning task. Trial timeline showing a 250 ms tone (auditory conditioned stimulus, CS), a 500 ms trace interval, and a 100 ms eyelid shock (unconditioned stimulus, US). EMG recordings from the orbicularis oculi muscle illustrate untrained (top) and trained (bottom) animals (note that the shock period saturates the EMG trace and is truncated here for visualization). Conditioned responses (CRs) are evident in trained animals prior to US onset.

c. Representative movement trajectories during conditioning sessions. Top: Gray traces depict the trajectory across the session during times where the animal is not performing the trace task. Bottom: Blue trajectories depict movement during the tone (CS), green during the trace, red during the shock (US), and black in the post shock period.

d. Example neuron showing rate maps during non-trace task (top left) and task (bottom left) periods. Task period is also represented as raster plots (top right) and peri-stimulus histograms (PSTH, bottom left) aligned to tone (CS) onset. Boxed graphs indicate figures corresponding to the trace task.

e. Same as d but for a different cell.

Hippocampal neurons encode distinct aspects of the trace task

To assess how hippocampal activity during the trace task differs from ongoing activity during free behavior, we quantified calcium event rates separately during trace task and non-trace task periods. At the population level, calcium event rates during the trace task were positively correlated with non-task rates (Fig. 2a), indicating that baseline firing tendencies were preserved across behavioral contexts. However, activity during trace task periods was systematically elevated, with most cells falling above the unity line. This increase was not driven by a small subset of highly active neurons but reflected a broad shift across the population (Fig. 2a; Fig. S3–4).

We next asked how many neurons exhibited significant task-related increases in activity.
. Comparing calcium event rates during the entire trace task window to intertrial periods revealed that 34.2 ± 8.2% of CA1 neurons exhibited significant task-enhanced activity relative to a shuffled null distribution (one-sided permutation test, $\alpha = 0.05$; Fig. 2b–c, Fig. S5–6). A smaller fraction (4.2% ± 2.8%) showed significant task suppression. This directional bias was evident at the population level, consistent with net recruitment of hippocampal cells during conditioning.

We then examined the temporal profile of task-modulated neurons. Among cells that were significantly modulated across the full trial window, responses were not uniformly distributed across the trial. Instead, most neurons showed peak modulation during a specific epoch (CS, trace, US, or post-shock), indicating temporally specific encoding rather than diffuse task engagement (Fig. 2c, Fig. S7). This demonstrates that neurons encoded specific epochs of the trace task rather than non-specific mechanisms such as altered arousal state.

Indeed, trace task-modulated neurons exhibited pronounced temporal heterogeneity. Distinct subsets of cells were preferentially active during the tone, trace, shock, or post-shock epochs, with relatively limited overlap across epochs (Fig. 2c–f, Fig. S7–S10). 85.7% of significantly modulated neurons were selective for one or two epochs, rather than being broadly active throughout the trial, indicating that task is neuronally structured in time. Although the post-shock period contained the largest absolute fraction of modulated cells, this epoch was also substantially longer than the others. After normalizing modulation by epoch duration, the density of post-epoch modulation was comparable to that observed during the tone and trace intervals and was exceeded by modulation during the brief shock epoch (Fig. 2c). Thus, the apparent dominance of post-epoch responses reflects window length rather than preferential recruitment.

136 Overlap analyses further showed that trace task-modulated activity was not restricted to a distinct cell
137 class (Fig. 2d). Task-selective and place-selective populations partially overlapped, consistent with the
138 idea that the trace task recruits neurons that may also participate in spatial coding. However, because
139 spatial tuning is examined in detail later (Fig. 4), we do not interpret this overlap here beyond noting
140 that task modulation is not confined to non-place cells.
141
142 Single-cell examples illustrate the heterogeneity of trace task-related responses (Fig. 2f). Some neurons
143 showed increased activity tightly aligned to the tone or shock, while others ramped during the trace
144 interval, and others exhibited delayed or prolonged post-US responses. Importantly, these trace task-
145 aligned calcium events occurred across a wide range of running speeds, suggesting that firing changes
146 were not trivially explained by locomotion.
147
148 Rats ran significantly faster during the trace task interval than during the pre-trial baseline (Fig. 2e–f; Fig.
149 S10–11), raising the possibility that increased activity was due to increased speed. However, speed–
150 firing correlations at both the trial level and within trials were near zero and indistinguishable from
151 shuffled controls (Fig. S12–13). Critically, when neural activity during trials was compared directly to
152 speed-matched intertrial periods, population-level calcium event rates remained significantly elevated
153 during the task (Fig. 2g). This effect was consistent across all animals and significant relative to a shuffled
154 null distribution. The same conclusion held at the single-cell level and was actually more pronounced:
155 most neurons fired 1.68x more during trials than during speed-matched non-task periods (Fig. 2h), an
156 effect that also persisted after controlling for acceleration (Fig. S14).
157
158 Together, these findings reveal that hippocampal neurons exhibit robust, heterogeneous task-related
159 increases in activity that occur independent of movement variables. The trace task engages a broad
160 subset of CA1 cells whose activity increases across multiple trace task epochs, with distinct temporal
161 profiles spanning the tone, trace, shock, and post-shock periods. These responses were not attributable
162 to locomotor speed and exceeded activity observed during speed-matched intertrial periods.
163 Thus, the trace task recruits a hippocampal ensemble in which task firing is not explained by motor
164 variables.
165

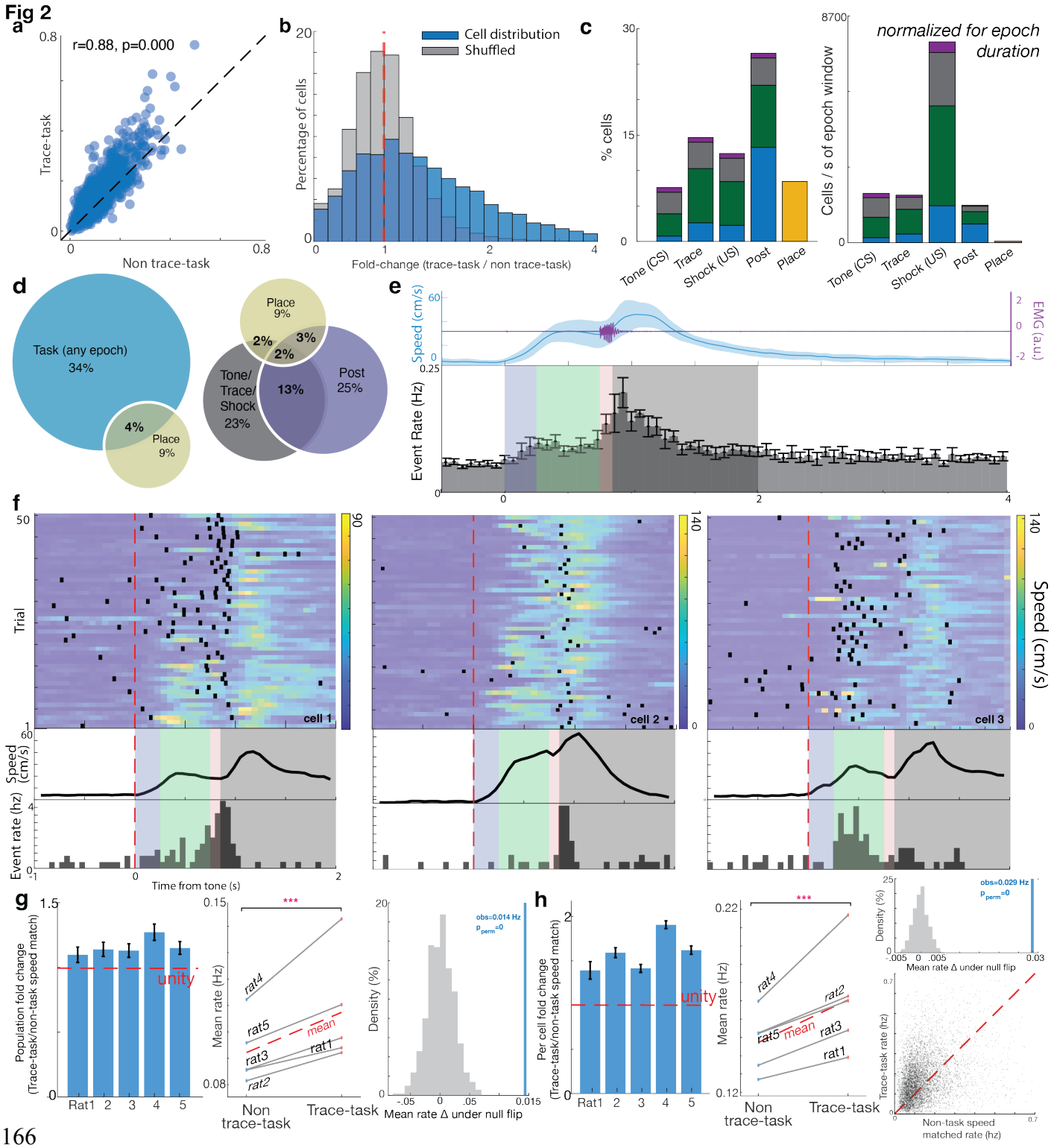

Fig 2.

a. Positive correlation between non-trial and trial calcium event rate pooled across all animals. Top figure shows raw calcium event rate in Hz. The dashed diagonal is unity (y = x), and the overlaid text gives Pearson's r and p-value. Note two outlier points are not on top figure for visualization purposes but are included in statistical analysis. See also figure S3 and S4.

b. Distribution of event rate change (trial / nontrial) across all recorded cells (blue) compared to a shuffled null distribution (gray). The dotted red line indicates no change (fold-change = 1). Modulation was biased toward increases, with 34.2 ± 8.2% of cells exhibiting significant task-enhanced activity (one-sided permutation test for increases, α

= 0.05). Plot ranges are set to the 99.5th percentile of pooled observed and shuffled values for visualization. See Fig. S5 for individual animals and Fig. S6 for the symmetric difference metric.

c. Among task-modulated cells (full-window significant), fraction with peak in each epoch; stacks show how many also have substantial modulation in +1/+2/+3 other epochs (by effect size). Top: For each task epoch (Tone/CS, Trace, Shock/US, Post) and for place, bars show the percent of cells significantly modulated (data normalized so that each rat contributes equally). Stacks partition each epoch's modulated population into cells modulated only in that epoch (blue) or additionally in +1 (green), +2 (gray), or +3 (purple) other epochs. This visualizes how strongly modulation is restricted to a specific epoch versus shared across multiple task periods. Right: The same counts normalized by epoch duration (cells per second of the epoch window). This compensates for large differences in window length (e.g., the short 100 ms shock epoch vs. the longer 1.15s post epoch) and reflects the density of modulation per unit time. Taller bars therefore indicate higher modulation rates independent of how long the epoch lasts. Also see figure S7 for same figure for place cells only; there was no significant difference between proportions for all cells and place cells (paired ttest, $p>0.05$, ks test $p>0.05$). See figure S8 for further breakdown by epoch using different methods.

d. Venn diagrams showing overlap of trace task selectivity and spatial selectivity (data is normalized so that each rat contributes equally). Left: Venn diagram shows percentage of cells modulated by trace task versus place. Right: Cell selectivity when 'tone+trace+shock' are treated as one epoch and 'post' as a separate epoch.

e. Top: Trial-aligned averages of running speed (blue, left y axis) and EMG activity (purple, right y axis) for across all sessions and all rats. EMG activity is purple and purple shaded areas denote ±1 standard deviation. Rats maintained locomotion throughout the trace period, with EMG responses reliably occurring before US delivery. See also figures S10 and S11. Middle, large peri-stimulus time histogram (PSTH): PSTH averaged across all rat, showing the average firing dynamics of CA1 neurons during trace conditioning. Each panel illustrates the mean firing rate (solid bars) in successive 133ms bins from 1s before to 2s after CS (tone) onset; error bars denote the SEM across cells. See figure S10 for individual animals and figure S11 for comparision of task vs pre task running speed.

f. Top row: Trial-by-trial raster plots (black dots) overlaid on trial-aligned speed heatmaps for three example neurons. Red dashed line indicates tone onset. Middle row: Average speeds across all trials for the represented day. Bottom row: PSTHs for the three pictured cells. Calcium events occurred across a wide range of speeds and cells were turned to different aspects of the task.

g. Comparison of population level mean calcium event rates during trace task periods versus speed-matched non trace task periods. Left: Fold change in firing rate (trace task / non-trace task, speed-matched) for each rat, shown as mean ± SEM for the population. The red line marks the across-animal mean. At the population level, there was on average 1.16x more calcium events during trials than during speed-matched controls, with individual rat means±std of 1.10 ± 0.04 1.14 ± 0.05 1.13 ± 0.05, 1.27 ± 0.06, and 1.15 ± 0.05. Middle: Per-rat mean calcium event rates during non-trial and trial periods; gray lines connect matched values from the same rat, and the red line indicates the across-animal mean. Across rats, calcium event rates were significantly higher during the trace task than in speed matched non-trial times (paired t-test, ***$p<0.001$). Right: Permutation test of the population mean Δ-rate (trial − non-trial). Histogram shows the null distribution obtained by random sign-flips across cells, and the blue line marks the observed mean (0.014hz), which lay far outside the null range ($p=0$). See figure S14 for analogous method used on acceleration data.

h. Comparison of calcium event rates for individual cells during trial periods versus speed-matched intertrial periods. Left: Fold change in firing rate (trace task / non-trace task) for each rat, shown as mean ± SEM across tested cells. The red line marks the across-animal

mean. Neurons had on average 1.68x more calcium events during trials than during speed-matched controls, with individual means±std of 1.39 ± 0.10, 1.59± 0.05, 1.41 ± 0.04, 1.91 ± 0.05, and 1.62 ± 0.05. Middle: Per-rat mean firing rates during non-trial and trial periods; gray lines connect matched values from the same rat, and the red line indicates the across-animal mean. Across rats, calcium event rates were significantly higher during the trace task than in speed matched non-trial times (paired t-test, ***$p<0.001$). Right top: Permutation test of the population mean Δ-rate (trial − non-trial). Histogram shows the null distribution obtained by random sign-flips across cells, and the blue line marks the observed mean (0.029hz), which lay far outside the null range (p=0). Right bottom: scatter plot comparing the trace task calcium event rate with the rate during speed-matched non-task periods. The majority of points fall above the unity line, indicating an overall higher rate during the trace task. See figure S15 for analogous method used on acceleration data.

The trace task evokes a temporally structured, trajectory-like population code

We next asked how the task organizes population activity. Comparing population vectors (PVs) across behavioral epochs showed that activity during the trace period was highly consistent from trial to trial and clearly distinct from non-task activity (Fig. 3a). Population similarity within the trace period was substantially higher than similarity between trace and non-task periods, or within non-task periods. This separation remained when non-task windows were selected to match the running speed profile of the trace period, indicating that differences in locomotor state alone do not explain the distinct population pattern observed during the task. Notably, speed-matched non-task activity was itself internally consistent, suggesting that both task and non-task behavioral states can support stable ensemble structure. However, the trace period was associated with a population configuration that was systematically different from non-task activity, reflecting a reproducible, trial-associated ensemble pattern.

To examine the organization within the trial, we divided the 0–2 s window into 15 temporal bins and computed similarity across split-averaged PVs. The across-rat similarity matrix showed a strong diagonal with banded off-diagonals, and lag–similarity curves decayed monotonically for every rat (Fig. 3b, S16-17). Population activity was also segmented by task epoch: within-epoch similarities exceeded between-epoch similarities across animals (Fig. 3b, S16-S17). These results indicate that the trial engages a conserved, temporally organized trajectory through population space.

We next asked whether this temporal trajectory mirrors the distance-dependent structure of spatial coding. Using equal-occupancy spatial bins, spatial PV similarity was highest for adjacent locations and declined with spatial distance, consistent with place coding (Fig. 3c, S18-S19). Strikingly, temporal and

spatial lag curves exhibited nearly identical shapes across a range of bin numbers (4-14 bins; Fig. 3d), and split-half analyses confirmed the reliability of both structures (S17, S19). This alignment shows that population similarity falls off with “distance” along the relevant axis—time during the task; space during exploration.

Together, these results reveal that trace conditioning engages diverse temporal coding strategies, including early CS-driven responses, trace-interval modulations, US rate increases, and sustained post-US changes. Despite this heterogeneity, population activity during the trial is highly stereotyped and distinct from non-trial periods, indicating the emergence of a structured ensemble code during the task. Together, these findings reveal that trace conditioning recruits a robust, temporally structured ensemble code that is distinct from non-trial activity yet geometrically analogous to the canonical distance code in space. This temporal–spatial alignment indicates a shared organizing principle for spatial and temporal hippocampal codes. In summary, the trace task restructures CA1 activity into a robust, temporally organized population code that is distinct from place coding.

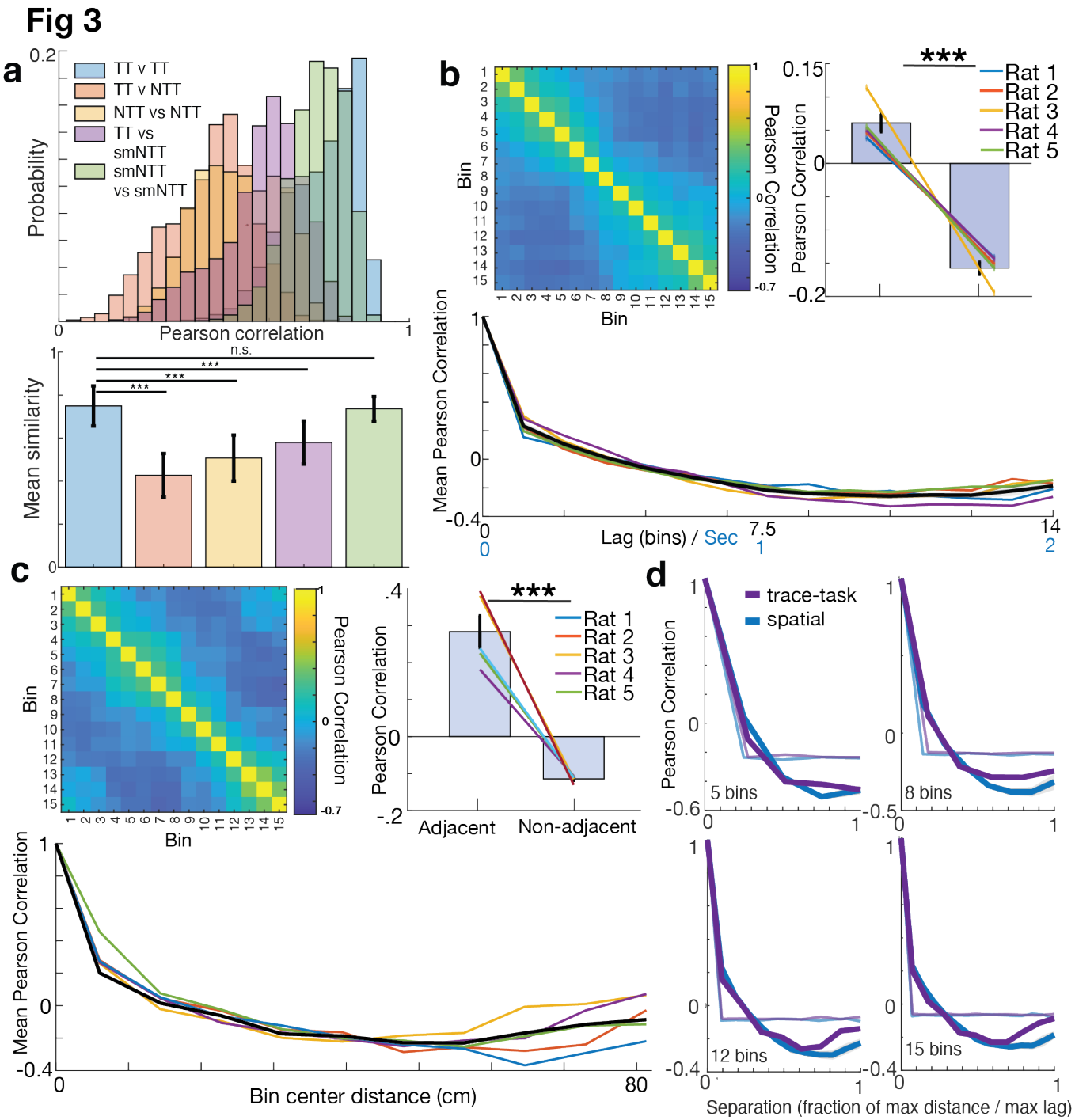

Figure 3. Heterogeneous but distinct neuronal dynamics and coding across trials

a. TT = trace task, NTT = non–trace task, smNTT = speed-matched non–trace task. Top, pooled bootstrap distributions across sessions. Bottom, session means ± SD. For each session (n = 15), per-trial 2-s trace task windows were compared with (i) randomly selected non-task windows and (ii) speed-matched non-task windows drawn strictly from outside the task window. For each bootstrap draw, trials were split into disjoint groups to form population vectors (PVs), and similarity was quantified as the Pearson correlation across cells. Trace task similarity (TT vs TT; 0.750±0.093) was substantially higher than trace task–non-task (TT vs NTT; 0.427±0.101), non-task–non-task (NTT vs NTT; 0.507±0.107), and trace task–speed-matched non-task (TT vs smNTT; 0.580±0.100) similarity (paired tests across sessions, ***$p < 0.0001$ for all comparisons). In contrast,

speed-matched non-task activity was internally reliable (smNTT vs smNTT; 0.736±0.057) and did not differ significantly from trace task similarity, indicating that the trace task organizes CA1 population activity into a consistent, trial-specific ensemble state distinct from non-task activity.

b. Population-vector similarity is strongly time-structured and shared across rats. Left, heat map: Across-rat mean similarity matrix (0–2 s after CS onset divided into 15 equal "splits"), population vectors were built from split-averaged event rates centered around their means and compared with Pearson correlation. Bright diagonal and banded off-diagonals indicate that population activity is most similar for nearby time bins and progressively less similar with temporal distance. Top right: within vs between epochs. Bins were grouped into CS, trace, US, and post-US epochs. Bars show across-rat mean (± SEM) similarity for all within-epoch pairs vs between-epoch pairs; colored lines are individual rats. Within-epoch similarity exceeded between-epoch similarity (Paired t test, p*** = <0.001 across rats and for each rat, see figure S16), indicating that activity is not only temporally smooth but also clustered by task epoch. Bottom, lag curves: For each rat (colored lines), mean similarity is plotted as a function of lag (difference in split index). Thick black line shows the across-rat mean ± SEM. All rats show a monotonic decay of similarity with lag, consistent with a temporally organized population code. (Fig. S16). Split-half analyses confirmed that lag structures were reliable within session (Fig. S17)

c. Spatial population similarity is structured by physical proximity. Left, heat map: Across-rat mean similarity matrix. Population vectors (PVs) were built from 15 equal-occupancy spatial bins computed from non-trial running epochs (speed ≥ 4 cm/s). PVs were built from per-cell mean event rates in each bin and centered around the mean per cell and compared with Pearson correlation. The bright diagonal and banded off-diagonals indicate strongest similarity for nearby bins that share borders. Top right: spatially adjacent bins vs non-adjacent bins (adjacency defined on the 2-D grid by rook/edge sharing). Bars show across-rat mean ± SEM; colored lines are individual rats. Adjacent bins were more similar than non-adjacent bins (Paired t test, p*** = <0.001 across rats and for each rat, see figure S18). Bottom, lag curves: For each rat (colored lines), mean similarity is plotted as a function of lag (distance of bin centers in cm.). Similarity generally decreases with physical distance, consistent with a distance-structured spatial code. Split-half analyses confirmed lag structures were reliable within session (Fig. S19)

d. Temporal and spatial population-vector similarity show a shared distance–decay profile. Population-vector (PV) similarity is plotted versus temporal lag during the task period (0–2 s; temporal, dark purple) and versus spatial separation during non-trial running (spatial, dark blue). Because spatial position is two-dimensional, spatial "lag" is expressed as distance between arena bins rather than the number of bin steps (for reference, one temporal lag bin corresponds to 0.13 s). Each panel shows a different discretization of time/space (5, 8, 12, or 15 bins; top-left to bottom-right). Solid lines show across-rat means. Faint purple and blue bands indicate shuffle/null references for temporal and spatial curves, respectively (mean of 500 bin-order permutations of the PV similarity matrix). In every binning scheme the temporal and spatial curves decline with lag and closely overlap in shape (Pearson r on curves: 0.990, 0.981, 0.975, 0.967 for 5/8/12/15 bins; RMSE_z = 0.123–0.246). The integrated magnitudes of the temporal and spatial curves did not differ from each other (ΔAUC permutation test, p = 0.866, 0.732, 0.624, 0.714 for 5/8/12/15 bins). Together, these analyses show that CA1 ensemble states obey a similar distance–decay rule in time during the trial and in space during exploration.

The trace task disrupts hippocampal spatial coding

To determine how task-related activity interacts with spatial representations in hippocampal CA1, we examined the impact of the trace task on spatial coding during free exploration. As expected, a subset of neurons exhibited spatially structured firing during non-task running, as quantified by spatial mutual information (MI) computed outside trial epochs (Fig. S20). Across animals, approximately 9% of cells exceeded a shuffled MI threshold, consistent with previous estimates of spatial tuning reported in calcium imaging studies during open-field exploration.

Including trace task activity altered spatial structure. Excluding task-period calcium events increased spatial mutual information across animals, whereas removing comparable activity from non-task periods had a smaller effect (Fig. S21). This indicates that task-locked activity disproportionately degrades spatial information, consistent with these events being temporally organized and only weakly related to the animal's position. Furthermore, this disruption persisted beyond the nominal trace interval. Spatial information remained reduced for several seconds following the unconditioned stimulus (Fig. S22), and trace-period activity was characterized by elevated trial-to-trial variability and reduced reliability relative to non-task running, despite higher mean firing rates (Fig. S23). Alternative information-theoretic measures yielded qualitatively similar results (Figs. S24–S25).

We next asked whether task-related responses were constrained by spatial position at the level of individual neurons. Trace-period firing rates did not differ between trials whose occupancy centroids fell inside versus outside a cell's non-task-defined place field (Fig. S26). Likewise, neither distance to the place-field center nor spatial separation between trials meaningfully predicted firing variability during the task (Figs. S27–S28). These results indicate that task-locked responses are largely uncoupled from spatial location.

Direct comparison of spatial firing patterns revealed a redistribution of activity during the trace task. Individual neurons frequently expressed calcium events outside their non-task-defined place fields during trials, as reflected by increased activity in task-defined spatial masks and, in some animals, reduced activity within non-task-defined place-field zones (Fig. S29). These results indicate that the task reshapes where neurons are active in space, rather than simply scaling pre-existing place fields.

At the population level, these effects exposed a pronounced asymmetry between task and spatial representations. Trial–trial population-vector (PV) similarity was only weakly influenced by spatial location: PV similarity was modestly higher for trials occurring at the same location than for those at different locations, and this effect was small and inconsistent across animals (Fig. 4b). A parallel single-cell split-half analysis yielded a similar result, with only weak spatial specificity of temporal task-

388 response profiles (Fig. 4c). Together, these analyses indicate that the task ensemble itself is not strongly
389 organized by space.
390
391 In contrast, spatial coding was robustly disrupted during the trace task. Spatial PV similarity for matched
392 locations was markedly reduced during the trace interval compared to non-task running, even when
393 both were referenced to the same non-task spatial template (Fig. 4e). This reduction was large,
394 consistent across animals and days, and highly significant relative to within-day permutation controls
395 (Fig. S30). A corresponding effect was evident at the single-cell level: correlations of per-cell spatial firing
396 patterns across spatial bins were strongly reduced during the task (Fig. 4f; Fig. S31), indicating a loss of
397 stable, location-specific firing within individual neurons. Additionally, averaging single-cell spatial
398 stability within each animal revealed a robust reduction during the trace task (Fig. 4g), indicating a loss
399 of stable, location-specific firing at the level of individual neurons; a corresponding reduction in spatial
400 stability was also observed in population-vector analyses (Fig. S32).
401
402 Together, these findings reveal a pronounced asymmetry between task and spatial representations in
403 CA1. Trace task activity is only weakly constrained by spatial location, whereas the trace task
404 substantially degrades spatial firing structure at both the single-cell and population levels. During trials,
405 neurons increase their firing and frequently have calcium events outside their established place fields,
406 leading to a degradation of spatial population structure. These results indicate that the task recruits a
407 mode of hippocampal processing that is largely distinct from classical spatial coding and can transiently
408 override it.

Fig 4

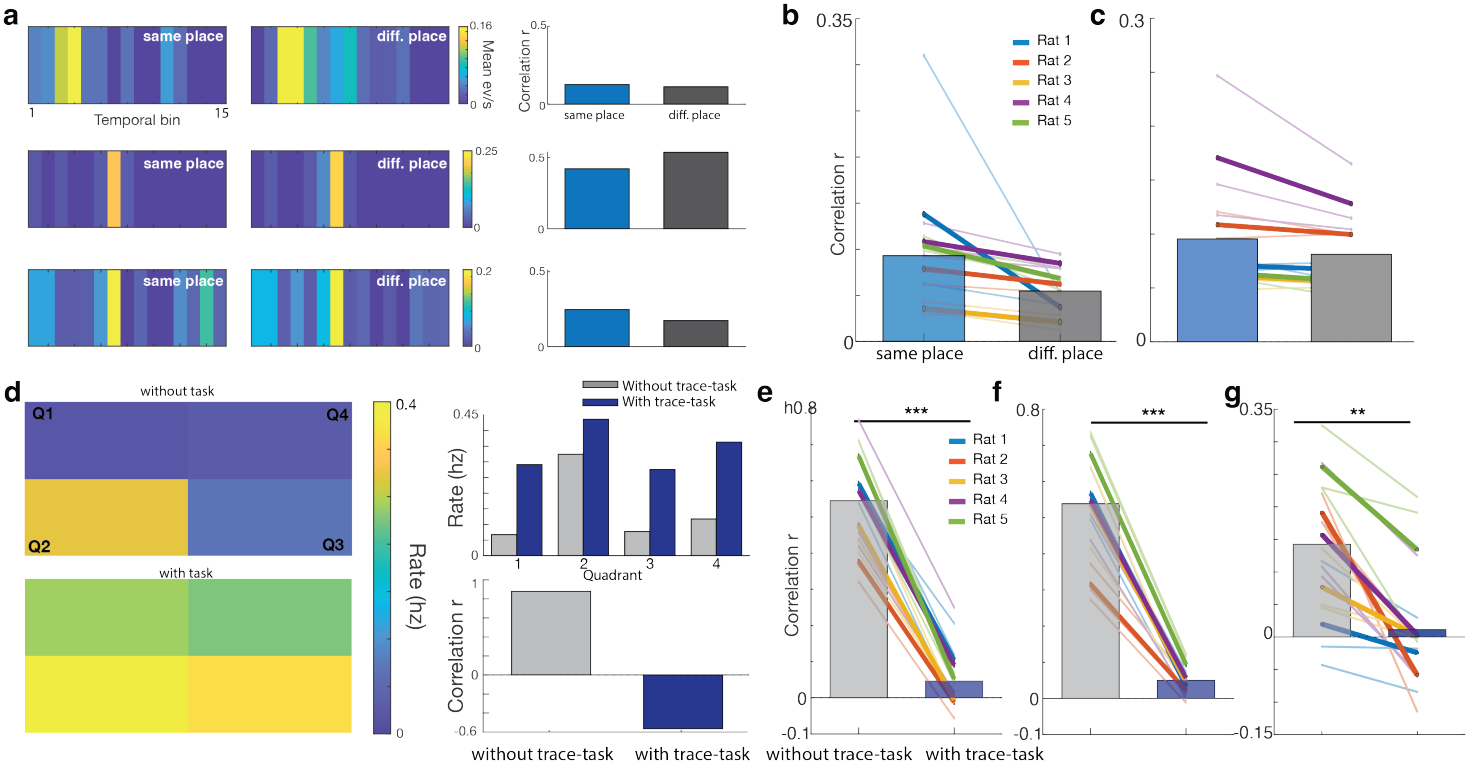

409

410

411

412 **Figure 4**

413 a. Example single-cell temporal activity profiles underlying split-half spatial similarity
414 analyses**.** Each row shows one hippocampal neuron from a representative recording day. Left
415 and middle: mean calcium event rate across temporal bins within the trace interval, computed
416 separately for trials in which the animal occupied the same spatial bin (left) versus different
417 spatial bins (middle). Right: mean across-trial correlation of temporal activity profiles
418 (Pearson r) for same-place and different-place comparisons. These examples illustrate how
419 trial-to-trial consistency of temporally structured activity can differ depending on spatial
420 context, motivating the population-level split-half similarity analyses shown in panels e–f.
421 b. Trial–trial population-vector (PV) similarity is compared for pairs of trials whose time-bin-
422 matched occupancy centroids occurred in the same vs different spatial locations. Bars show
423 across-day means (n=15 days from 5 rats); thin lines connect paired day means colored by
424 rat. PV similarity was not signigicantly higher for trials occurring in the same location
425 compared with trials occurring in different locations when assessed across animals (paired t
426 test in Fisher z space, $t(4) = 2.37$, $p>0.05$). PV similarity was modestly but significantly
427 higher for trials occurring in the same location compared with trials occurring in different
428 locations when assessed across days (paired t test in Fisher z space: $t(14)=2.30$, $p=0.04$).
429 c. Single-cell split-half spatial specificity during the task period. Trial-to-trial similarity of
430 single-cell temporal activity profiles was compared for pairs of trials occurring in the same
431 spatial bin versus different spatial bins. Similarity was quantified as the Pearson correlation
432 of per-cell temporal activity vectors across split halves, Fisher-z transformed and averaged
433 within day. Across animals (n = 5), same spatial bin correlations were higher than different
434 bin correlations but did not reach statistical significance (paired t test in Fisher z space,
435 $t(4)=1.96$, $p>0.05$). Across days (n = 15), same spatial bin similarity was modestly but
436 significantly higher than OUT–OUT (paired t test in Fisher z space, $t(14)=2.44$, $p<0.05$).
437 Bars show means; thin lines indicate paired day values colored by animal.

d. Single-cell example illustrating the spatial-stability metric used in population analyses. Left: Spatial firing-rate maps from one neuron during non-task exploration (top; reference map) and during the trace task (bottom). Each square corresponds to one spatial quadrant of the arena; color indicates mean firing rate (Hz) on a shared scale. Right: Quadrant-averaged firing rates (top) and spatial similarity (bottom), computed as the Pearson correlation across quadrants between activity vectors. In the absence of the task, the neuron exhibited a spatially structured firing pattern with high within-map similarity. During the trace task, firing became more uniformly distributed across space, yielding reduced spatial similarity. This single-cell example mirrors the correlation-based spatial-stability measures computed across neurons and days in the subsequent analyses.

e. Spatial PV similarity for the same locations was compared between the trace task and non-task running. For each day, population vectors were computed as mean activity within coarse spatial bins. Without-task stability was defined as the correlation between PVs from two independent halves of non-task data, while with-task similarity was computed by correlating trace-interval PVs to a non-task spatial template from the same day. Values reflect averages across Monte Carlo resamples computed in Fisher-z space and converted back to r for visualization. Spatial similarity was significantly lower during the task trace interval than during non-task periods (mean r: 0.050 task vs 0.54 non-task). This reduction was robust across animals (paired t-test in z space: $t(4)=-10.10$, $p<0.00$) and across days (paired t-test in z space: $t(14)=-13.81$, $p<0.001$). Within each animal, significance was confirmed using a within-day sign-flip permutation test on paired bin-wise differences (two-sided $p\leq0.001$ for all animals; see Fig. S30).

f. Single-cell spatial reliability was compared between the trace task and non-task running. For each neuron, spatial firing maps were constructed across coarse spatial bins. Without-task reliability was defined as the correlation of each cell's spatial map across independent non-task subsets, whereas with-task reliability was quantified by correlating each cell's task-epoch spatial map with its non-task spatial template from the same day. Correlations were Fisher-z transformed and averaged within day and animal before visualization. Single-cell spatial similarity was markedly reduced during the trace task compared to non-task periods (mean r: 0.050 task vs 0.530 non-task), indicating disruption of location-specific coding at the level of individual neurons. This effect was significant across animals (paired t-test in z space: $t(4)=-7.96$, $p^{***}=0.001$) and across days (paired t-test in z space: $t(14)=-12.07$, $p<0.001$). Significance was further supported by within-animal, day-aware sign-flip permutation tests (all rats $p\approx0$; see Fig. S31).

g. Single-cell spatial stability is reduced during the trace task. Spatial stability was quantified for each neuron as the Pearson correlation of its spatial firing pattern across arena bins, computed separately during non-task and task epochs. For each animal, single-cell correlations were averaged across neurons and days. Points show per-animal means (bold colors), lighter lines indicate individual days, and bars show across-animal means. Single-cell spatial similarity was significantly lower during task compared to non-task epochs (mean r: 0.314 vs 0.557; rat-averaged Fisher z: 0.325 vs 0.628), indicating task-associated disruption of spatial firing structure at the level of individual neurons. This effect was significant across animals (paired t-test in Fisher z space: $t(4)=4.392$, $p^{**}=0.01$, n=5 rats) and across pooled day pairs ($t(14)=4.805$, $p<0.001$ n=15 days). See Fig. S32 for the corresponding population-vector analysis.

Discussion

The trace task reorganized hippocampal CA1 activity into a dominant, temporally structured population response that was less constrained by spatial location. Across animals, task-related population structure exceeded spatial coding in magnitude, and individual neurons exhibited heterogeneous, epoch-specific responses across the tone, trace, shock, and post-shock periods. Despite this single-cell diversity, population activity cohered into a consistent trajectory that was distinct from non-task activity and internally organized by task time. At the same time, spatial coding was transiently disrupted: place-related firing became less reliable, and spatial similarity decreased at both the single-cell and population levels. Together, these findings show that during active behavior, hippocampal coding can be reorganized by task demands into a non-spatial population response that disrupts classical place coding.

Reports that hippocampal task responses appear gated by place fields have been interpreted as evidence that non-spatial signals in CA1 are secondary to spatial coding[6,7,37]. Our results instead show that such place-bound task responses arise under restricted behavioral conditions. When animals are immobile or task events occur at fixed sites or within a limited set of locations, trials are sampled from a narrow spatial range, causing task-related activity to appear place-gated because spatial variation is not tested. In contrast, when animals remain mobile and task events are sampled across the environment, the trace task recruits a temporally organized population response that reduces spatial reliability rather than reinforcing it. Notably, even on trials preceded by brief immobility, we did not observe stable place-specific firing during task periods. Thus, whether task responses appear spatially gated or spatially disruptive reflects behavioral state and spatial sampling, rather than a fixed or obligatory relationship between task responses and spatial coding (Box 1).

Additionally, despite their distinct organizing variables, task-related and spatial population structure obeyed a similar distance–decay relationship. Population similarity decreased with increasing temporal separation during the task and with increasing spatial separation during exploration, and the shapes of these decay functions closely overlapped (Fig 3d). This correspondence indicates that task and spatial coding share a common population-level geometry, even as different dimensions dominate under different behavioral demands. The trace task therefore recruits an existing population structure rather than introducing a separate representational mode.

515 Taken together, these results reveal three core features of hippocampal coding during trace
516 conditioning. First, task-related population structure exceeds spatial coding in magnitude
517 during active behavior. Second, the trace task reduces spatial reliability, demonstrating that
518 task coding is not simply layered onto stable place representations. Third, task and spatial
519 coding share a common distance–decay structure, indicating a shared population geometry.
520 Apparent disagreements in the literature may therefor arise from differences in
521 whichdimension (space or task time) dominates in a behavioral task. Our findings extend the
522 classical view of the hippocampus as a primarily spatial map toward a flexible population code
523 that prioritizes behaviorally relevant structure across time and space.

524

Prior task paradigms	**This study**
Fixed stimulus location or trials tend to happen at specific locations such as endpoints[37]	Random trial locations (Fig 1)
Long CS or repeated US[38]	Brief CS-trace-US structure (Fig 1)
Reward linked endpoints[37] or rewarded field[38]	No reward (Fig 1)
Non-hippocampally dependent task (e.g. no trace period)[38]	Hippocampally dependent task[29]
Freezing at trials[38]	No freezing at trials (Fig 2)
Electrical artifact during US limits reliable recording of hippocampal activity during shock[37]	Calcium imaging permits continuous measurement through CS, trace, US, and post-US epochs
Observed outcome: Task responses appear gated by place fields when spatial and task signal align	**Observed outcome:** Temporally structured task ensemble (Figs. 2–3) accompanied by reduced spatial stability (Fig. 4)
Whether hippocampal task responses appear spatially gated or spatially disruptive depends on behavioral state and spatial sampling, reflecting flexible coding rather than a fixed place-only representation[11].	

525 **Box 1 | Behavioral and methodological factors that determine whether hippocampal task**
526 **responses appear place-bound.**
527 Prior reports of place-gated task responses can arise from restricted spatial sampling,
528 immobility, reward structure, or limited access to brief task epochs. When these constraints are
529 removed, the task recruits a temporally structured population response that reduces spatial
530 stability

531

532

533

534

535

536 **Methods**

537 **LEAD CONTACT**

538 Questions and requests for information should be directed to and will be fulfilled by the Lead
539 Contact, Hannah Wirtshafter (hsw@northwestern.edu). This study did not generate new unique
540 reagents.

541

542 **DATA AVAILABILITY**

543 The data that support the findings of this study are available from the corresponding author. All code
544 produced for data analysis is available on https://github.com/hsw28/ca_imaging

545

546 **EXPERIMENTAL MODEL AND SUBJECT DETAILS**

547 All procedures were performed within Northwestern Institutional Animal Care and Use
548 Committee and NIH guidelines. Five male Long Evans rats (275–325 g) were sourced from Charles River
549 Laboratories, injected with AAV9-GCaMP8m, implanted with a 2-mm GRIN lens, and trained and tested
550 on eyeblink conditioning in a rectangular apparatus (Fig. 1). Animals were individually housed in an
551 animal facility with a 12/12 h light/dark cycle.

552

553 **METHOD DETAILS**

554 **GCaMP8 injection, lens implantation, EMG implantation**

555 GCaMP8 injection and lens implantation were completed as reported in Wirtshafter and
556 Disterhoft, 2022 and Wirtshafter and Disterhoft, 2023, and Wirtshafter, Solla, and Disterhoft, 2024[17,42,43].
557 Briefly, rats were anesthetized with isoflurane (induction 4%, maintenance 1-2%) and a craniotomy was
558 performed at stereotaxic coordinates Bregma AP −4.00mm, ML 3.00mm. 0.06uL of GCaMP8m (obtained
559 from AddGene, packaged AAV9 of pGP-AAV-syn-jGCaMP8m-WPRE, lot v175525, titer 1.3E+13 GC/mL)
560 was injected over 12 minutes (approximate coordinates Bregma AP −4.00mm, ML 3mm, DV 2.95mm
561 relative to skull); then the syringe was raised 0.2mm and an additional 0.6ul of GCaMP7 was injected.
562 We repeated this process once more and at slightly different coordinates in the craniotomy hole,
563 resulting in 4 total injections.

564 We then aspirated tissue from the craniotomy site using a vacuum pump and 25 gauge needle.
565 Tissue was aspirated up to and including the horizontal striations of the corpus collosum. A 2mm GRIN
566 lens (obtained from Go!Foton, CLH lens, 2.00mm diameter, 0.448 pitch, working distance 0.30mm,
567 550nm wavelength) was then inserted into the craniotomy hole and cemented in place using dental
568 acrylic. Animals were given buprenorphine (0.05mg/kg) and 20mL saline, taken off anesthesia, and
569 allowed to recover in a clean cage placed upon a heat pad.

570 Six to eight weeks after surgery, animals were again anesthetized with isoflurane and checked
571 for GCaMP expression. If expression was seen, baseplates were attached using UV-curing epoxy and

572 dental acrylic. Electrode implantation to record obicularis oculi electromyographic (EMG) activity
573 occurred in the same surgery as baseplate attachment, as described previously[44,45]. Briefly, a connector
574 containing 5 wires was cemented on the front of the animal's head: 4 wires were implanted directly
575 above the eye in the surrounding muscle (2 for recording, 2 for electrical stimulation). An additional wire
576 was attached to a connector attached to a ground screw located above the cerebellum; this screw was
577 implanted during lens implantation surgery.
578
579 **Behavioral environment and training**
580 A single behavioral apparatus was used in these experiments. The environment was a 78.7cm x
581 50.8cm unscented rectangular enclosure with wire floor and walls and white lighting. A tether
582 containing a plug to relay the EMG activity and to deliver a shock to the rat's eye was attached to a the
583 eyeblink connector on the rat's head. The miniscope was plugged into the cemented baseplate. The
584 miniscope and EMG cords were all attached to a commutator for ease of animal movement.
585 The CS was a 250ms, 85dB free-field tone (5ms rise-fall time). The US was a 100ms shock
586 directed to the left eye. Shock amount varied per session per animal and was calibrated, if needed, at
587 the end of a training session for the next session's training. Shock level was deemed appropriate when a
588 shock was met with a firm shake of the animal's head.
589 The trace interval was 500ms and the intertrial interval (ITI) was randomized between 30s and
590 60s, with a 45s average. EMG signal output was amplified (5000×) and filtered (100 Hz to 5 kHz), then
591 digitized at 3 kHz and stored by computer.
592 A conditioned response (CR) was identified as an increase in integrated EMG activity that
593 exceeded the baseline mean amplitude by more than four standard deviations, sustained for a minimum
594 duration of 15ms. Baseline mean amplitude was calculated during the 500ms preceding CS onset.
595 Additionally, the response had to commence at least 50ms after the conditioned stimulus (CS) onset and
596 before the unconditioned stimulus (US) onset.
597 The animal's first exposure to each environment was a 38min exploration session, in which the
598 animal was able to freely move and explore the environment without any conditioning (Figure 1a).
599 Animals were then trained in one environment per session, with no more than one session per day, and
600 were considered to have learned the task after reaching criterion (70% CRs in 50 trials) on three
601 consecutive training sessions (termed 'criterion sessions').
602
603 **Calcium imaging**
604 Calcium imaging was completed as reported in Wirtshafter and Disterhoft, 2022 and Wirtshafter
605 and Disterhoft, 2023, and Wirtshafer, Solla, and Disterhoft 2024[17,42,43]. Briefly, calcium imaging was done
606 using UCLA V4 Miniscopes[46,47], assembled with two 3mm diameter, 6mm FL achromat lens used in the
607 objective module and one 4mm diameter, 10mm FL achromat lens used in the emission module.

608

609 **QUANTIFICATION AND STATISTICAL ANALYSIS**

610 Unless otherwise noted, means are reported as mean ± standard deviation. All analyses exclude cells
611 with fewer than five calcium events across all trial periods. For multi-animal comparisons, averages were
612 computed by first calculating the relevant metric per animal and then averaging across animals, rather
613 than pooling across sessions or cells. The exception is population-level analyses in Fig. 3, which were
614 computed across all cells. All statistical tests are two sided. All analysis and figure-generation code is
615 available at https://github.com/hsw28/ca_imaging.

616

617 **Position and speed analysis**

618 Position was sampled by an overhead camera at 30Hz. Position tracking was done post-
619 recording using DeepLabCut[48]. Position was then converted from pixels to cm. Position was smoothed
620 using a Gaussian filter with standard deviation of 2cm. Speed was calculated by taking the hypotenuse
621 of the coordinates one before and after the time of interest.

622

623 **Video pre-processing and cell identification**

624 Video pre-processing and cell identification were performed as reported in Wirtshafter and
625 Disterhoft, 2022, Wirtshafter and Disterhoft, 2023, and Wirtshafter, Solla, and Disterhoft, 2024[17,42,43]. In
626 brief, videos were recorded with Miniscope software at 15frames/second. Video processing was done
627 using CIATAH software[49]. Videos were down sampled in space and normalized by subtracting the mean
628 value of each frame from the frame. Each frame was then normalized using a bandpass FFT filter (70-
629 100cycles/pixel) and motion corrected to a using TurboReg[50]. Videos were then converted to relative
630 florescence (dF/F_0); F_0 was the mean over the entire video.

631 Cells were automatically identified using CIATAH[49] using CNMF-E[51]. Images were filtered with a
632 gaussian kernel of width 2 pixels and neuron diameter was set at a pixel size of 8. The threshold for
633 merging neurons was set at a calcium trace correlation of 0.65; neurons were merged if their distances
634 were smaller than 4 pixels and they had highly correlated spatial shapes (correlation>0.8) and small
635 temporal correlations (correlation <0.4).

636 All cells identified using CNMF-E were then scored as neurons or not by a human scorer. Scoring
637 was also done within CIATAH software in a Matlab GUI. Scoring was done while visualizing and
638 considering a calcium activity trace, average waveform, a montage of the candidate cell's Ca2+ events,
639 and a maximum projection of all cells on which the candidate cell was highlighted. The relative
640 fluorescence ($\Delta F/F_0$) local maxima of each identified cell were considered calcium event times.

641 We recorded a total of 6,664 cells across 15 sessions, three sessions per rat (average of
642 205 ± 51, 339 ± 169, 242 ± 21, 777 ± 121, and 658 ± 213 cells per rat). All analyses included only cells
643 with either a calcium rate in non-trial periods of at least 0.05hz or a trial period calcium event rate of at

644 least 0.05h. This resulted in a final dataset of 6192 cells, with an average of 179±34, 328±163, 220±2,
645 732±130, and 603±203 cells per animal.
646
647 **Task modulation analysis (conditioning vs intertrial).**
648 Trial-period activity was defined as the 0–2 s window following CS onset. All other time points
649 were considered non-trial periods unless otherwise noted. Task modulation was quantified as the ratio
650 of mean activity during the conditioning window to mean activity during the intertrial interval.
651 Significance was assessed by comparing the observed modulation value for each neuron to a null
652 distribution generated by permuting trial and intertrial labels 500 times.
653 In a complementary analysis, symmetric-difference modulation was computed as:
654 $$\frac{r_{task} - r_{basline}}{r_{task} + r_{basline}}$$
655 Where
656 $$r_{task} = mean\ event\ rate\ during\ trial\ periods$$
657 $$r_{basline} = mean\ reate\ during\ nontrial\ periods$$
658
659 **Firing rate comparisons.**
660 We first computed per-neuron calcium event rates during the trace window and during
661 randomly sampled non-task windows of equal duration. We compared the distribution of firing rates
662 across conditions using a two-sample Kolmogorov–Smirnov (KS) test and a paired t-test. Population-
663 level differences in mean event rate were visualized using histograms and bar plots of mean ± SEM.
664
665 **Modulation Clustering by Epoch**
666 To identify neurons with selective modulation during different phases of the trace-conditioning
667 trial, we computed firing-rate changes relative to baseline in four task epochs: conditioned stimulus (CS;
668 0–250 ms after tone onset), trace interval (250–750 ms), unconditioned stimulus (US; 750–850 ms), and
669 a post-US period (850–2000 ms). Baseline activity was calculated from a pre-trial window (−2–0 s
670 relative to CS onset) for each neuron and trial. For each neuron, we computed modulation indices for
671 each epoch as:
672 $$\Delta = \frac{\mathrm{r_{epoch}} - \mathrm{r_{baseline}}}{\mathrm{r_{epoch}} + \mathrm{r_{baseline}} + \in}$$
673 Where:
674 $$\mathrm{r_{epoch}} = mean\ calcium\ event\ rate\ during\ epoch\ period$$
675 $$r_{baseline} = mean\ calcium\ event\ rate\ during\ baseline\ period$$
676 $$\in = 10^{-5}$$
677 Because CS (250 ms) and US (100 ms) are short relative to our 133 ms frame, very low counts
678 inflate variance and can saturate delta. To ensure well-estimated rates, we included cells with ≥5 total

events across all trials in the 0–2 s task window OR ≥5 baseline events (−2–0 s). This criterion is direction-agnostic (does not favor excitation) and was chosen based on stability diagnostics. As a robustness check, we repeated the analysis using PSTHs with data centered around the mean (and obtained the same directional effects (Fig. S10).

The resulting four-dimensional modulation vectors (Δ values) from all neurons underwent k-means clustering (k = 4, 10 replicates, MATLAB Statistics Toolbox) to identify functional response classes. Clusters were reordered such that those with maximal CS modulation were plotted first, followed by trace, US, and post-US groups. Heat maps display individual neuron modulation indices sorted first by dominant epoch and then by response sign. For each cluster, mean ± SEM Δ values were plotted, and cluster prevalence was calculated separately for each animal and as an across-animal mean. For the epoch defining each cluster, we also quantified the proportion of neurons with positive versus negative modulation.

Sliding-Window Latency Analysis

To determine the latency of task-related neuronal recruitment, we performed a sliding-window analysis of peristimulus activity. For each neuron, spike times were aligned to CS onset and binned into non-overlapping windows of 133 ms (reflecting the calcium imaging sampling rate of 7.5 Hz) from 1 s before CS to 2 s after CS onset. For each trial, we computed baseline activity as the mean firing rate during the pre-CS window (−5–0 s). Each post-CS bin was compared to the baseline distribution across trials using a paired t-test ($\alpha = 0.05$). False discovery rate (FDR) correction was applied within each neuron to control for multiple comparisons. The latency of recruitment was defined as the first post-CS bin showing significant deviation from baseline.

Histograms of recruitment latencies were generated for each rat as well as across the full dataset. Cumulative recruitment curves quantified the fraction of significantly modulated neurons recruited as a function of time, enabling comparison of fast CS-locked responses and slower trace-interval responses.

Population state shift analysis

To compare task-period activity with post-trial activity relative to baseline running, we quantified population-vector (PV) similarity to a running-only template. For each animal, we identified the last up to three pre-conditioning days and analyzed each day separately before combining them with trial-count weighting. Calcium event trains were converted to instantaneous firing-rate vectors aligned to the position timestamps. Periods of running were identified by thresholding the instantaneous speed (≥4 cm/s). For each day, a “running template” PV was obtained by averaging activity across all running epochs that did not overlap with any CS-to-US window. For each trial, PVs were computed in two windows: a task epoch (0–0.85 s after CS) and a post-trial epoch (0.85–2.0 s after

CS). Trials with insufficient running within either window were discarded. PV similarity to the running template was measured using cosine similarity (default) or Pearson correlation. Pre- and post-trial similarities were averaged within day and then combined across days using weights proportional to the number of included trials. For sliding-state analyses, PVs were computed in 25 contiguous bins spanning –2 to +4 s relative to CS onset, with similarity to the running template computed for each bin when running duration exceeded a minimum threshold. This produced a time-resolved trajectory of state similarity surrounding the CS. Group statistics were calculated across animals using paired tests on per-animal similarity estimates.

Post-epoch peak-time analysis

To determine whether post-epoch–modulated neurons exhibited temporally anchored responses at trial offset, we quantified the timing of each cell's maximal post-epoch activity using a trial-averaged peri-stimulus time histogram (PSTH). For each rat, calcium event timestamps were converted into continuous firing-rate estimates (7.5 Hz sampling). For every trial, firing rates were extracted during the post-epoch window (0.85–2.0 s after CS onset), and times were converted to a relative coordinate spanning 0→1.15 s from post-window onset. These relative-time segments were binned at 0.133hz and averaged across trials to obtain a PSTH for each cell. PSTHs were smoothed with a Gaussian kernel (3 bins). Peak times were defined as the location of the PSTH maximum; when the maximum occurred away from bin edges, the peak time was refined by a three-point quadratic fit. Peak times were computed only for cells classified as post-modulated by the epoch-labeling procedure and were expressed in seconds from post-window onset. Within each rat, an empirical cumulative distribution function (CDF) of peak times was computed, and a cross-rat mean CDF was obtained by interpolating each rat's CDF onto a shared temporal grid. This analysis returns the temporal distribution of peak firing within the post-epoch and tests whether responses are concentrated immediately after trial termination or distributed throughout the window.

Speed Modulation Across Trials

To test whether calcium event rates were modulated by running speed at the trial level, we calculated the Pearson correlation between mean speed and mean calcium event rate across trials (defined over the 0–2 s window following CS onset) for each neuron. Mean speed was computed within the 0–2 s window following CS onset, matching the trace interval. Neurons with fewer than five total calcium events across all trials were excluded. To assess significance, we applied a false discovery rate (FDR) correction (q = 0.05) to each animal's set of correlation p-values. Additionally, we compared the observed correlations to a shuffled null distribution in which trial speeds were randomly permuted 500 times, recalculating the correlation for each permutation. Neurons whose observed correlation

exceeded the 95th percentile of the shuffled distribution were considered significantly speed-modulated.

Speed Modulation Within Trials

To assess whether calcium activity was modulated by moment-to-moment speed fluctuations within trials, we binned the 0–2 s post-CS window into 7.5 Hz time bins and computed the Pearson correlation between binned speed and calcium event rate within each trial. Each neuron's per-trial correlations were then averaged across trials. Neurons with fewer than five total events were excluded. Statistical significance was assessed using an FDR correction (q = 0.05) across the population. As a control, we generated shuffled speed vectors by randomly permuting the speed values within each trial and recomputed the correlations 500 times; the fraction of neurons exceeding the 95th percentile of this null distribution was used to estimate the false positive rate.

Speed-Matched and Acceleration-Matched Comparison of Task and Non-Task Activity

We quantified whether hippocampal neurons changed their firing during the task window relative to non-trial periods while explicitly controlling for running speed. "Trial" time was defined as the window from CS onset to 2 s post-CS (0–2 s). "Non-trial" comprised all other times in the session. For speed matching, non-trial periods were selected such that their instantaneous speeds closely matched the speed distribution observed during trials, using fixed-width speed bins. Acceleration was computed as the first derivative of speed and used analogously for acceleration-matched controls.

To match firing rates across comparable speeds, we partitioned time into speed bins with fixed width 2 cm/s, wherein the bin edges spanned the min–max speed observed within the trial window, and those same edges were applied to both trial and non-trial data. For each speed bin, we formed the union of contiguous time segments belonging to that bin separately for trial and non-trial, and computed the duration-matched firing rates as spike counts divided by the total time in those segments. Cells were tested if they had at least one eligible paired bin, and bins with zero rate on both sides were excluded; parameters were selected to include the maximum number of cells (n=6192). A paired test across all cells was then used to compare each cell's mean trial versus mean non-trial rate.

As a population-level control, we implemented a shuffle test: for each cell's per-bin rate differences (trial − non-trial), we randomly flipped the sign of each bin difference and recomputed the mean across bins. Repeating this procedure 500 times yielded a null distribution of mean Δ-rates under the hypothesis of no systematic difference. The observed mean Δ-rate was compared to this distribution to obtain a permutation p-value.

The same steps were used for acceleration matching except acceleration was binned in 3cm/s^2 bins rather than speed.

786 **Population vector similarity**

787 We quantified the structure of population activity during the trace window using a bootstrap
788 grouping analysis of population firing-rate vectors. For each session, firing-rate matrices were
789 constructed for all trace task trials by computing each neuron's event rate within the 0–2 s post-CS
790 window. To assess population similarity, we repeatedly drew two non-overlapping groups of trials (25
791 trials per group) and averaged firing rates across trials within each group to obtain two population
792 vectors. Similarity between group-averaged vectors was quantified using Pearson correlation across
793 neurons.

794 For non-task comparisons, we sampled 2 s windows drawn from periods that did not overlap
795 any trace windows. For analyses controlling for locomotor confounds, speed-matched non-task windows
796 were additionally selected by matching the within-window speed profile of each trace trial to candidate
797 non-task windows using a binned speed-profile distance metric.

798 This procedure yielded five within-session similarity measures: trace–trace, non-task–non-task,
799 trace–non-task, trace–speed-matched non-task, and speed-matched–speed-matched. For each metric,
800 bootstrap resampling was repeated 500 times per session to generate similarity distributions, and
801 session means were used for statistical comparisons. All similarity analyses were performed within
802 session, and sessions were weighted equally in pooled summaries (Fig. 3a).

803 Temporal structure during the trial: For temporal structure analyses (Fig. 3b, S17), the 0–2 s trial
804 window was divided into 15 equal bins aligned to imaging frames. For each bin, PVs were computed by
805 averaging event rates across included frames. Pairwise Pearson similarity across bins produced a
806 temporal similarity matrix per day. Lag–similarity curves were generated by averaging entries along
807 successive matrix diagonals. Task-epoch segmentation was assessed by grouping bins corresponding to
808 CS, trace, US, and post-US epochs (Fig. 3b, S16–S17).

809 Spatial structure during non-trial running: For spatial analyses (Fig. 3c, S18–S19), non-trial
810 running frames (speed ≥ 4 cm/s) were partitioned into equal-occupancy spatial bins. PVs were
811 computed for each spatial bin using the same normalization as temporal PVs. Pairwise Pearson
812 similarities across spatial bins formed a spatial similarity matrix, and spatial lag–similarity curves were
813 derived analogously.

814 Reliability of temporal and spatial structure was assessed using even–odd split-half analyses (Fig.
815 S17, S19). Lag curves from each split were correlated to confirm within-session consistency.

816

817 **Lag–similarity analysis**

818 For the lag–similarity analysis (Fig. 3d), temporal and spatial similarity matrices were reduced to
819 lag–similarity curves by averaging entries along their diagonals. To visualize a locality-free baseline, we
820 generated null curves by permuting the joint row/column order of each similarity matrix 500 times and
821 recomputing lag curves.

To compare temporal and spatial organization directly, lag–similarity curves were centered around the mean and their correspondence quantified using Pearson correlation and RMSE across bins. Differences in overall magnitude between temporal and spatial curves were tested using permutation tests on the difference in area under the curve (ΔAUC). Analyses were repeated across multiple bin numbers (4–14 bins) to verify robustness.

Place cell identification, computing spatial mutual information, and computing bits per second

Place cells were identified using mutual information computed when the animals were running at speeds greater than or equal to 4cm/s (. MI was computed for all cells; there was no calcium event rate criterion for included cells. To be considered significant, the computed mutual information (MI) must be greater than 95% of MI scores computed 500 times from shuffled positions[52]. To compute the MI for each cell, the training environments were divided into 2.5cm x 2.5cm bins. The calcium event rate of each cell and the occupancy of the animal were found for each bin. Rate and occupancy were smoothed with a Gaussian kernel with filter width of 3cm and Sigma of 0.5cm. Mutual information was computed during periods of movement as follows[43,52,53]:

$$p = \frac{P_s}{P_o}$$

$$M_s = \sum P_s$$

$$M_o = \sum P_o$$

$$MI = \sum p * \log_2\left(\frac{p}{M_s * M_o}\right)$$

where:

$$P_s = \text{calcium event probability in each bin}$$

$$P_o = \text{occupancy probability at each bin}$$

For all spatial MI analyses reported in the Results, MI was computed using only non-trial data, excluding the 0–2 s window following each CS onset.

To quantify how task-period calcium events influence spatial information, we recomputed MI including the 0–2 s trial window. Including trial periods consistently reduced MI in every animal, indicating that trial-locked activity tended to be non-spatial.

To ensure this reduction was not driven solely by loss of event count, we performed a spike-matched control: for each neuron we removed the same number of calcium events as occurred in the 0–2 s window but sampled them at random from all high-velocity non-trial events. MI was then recomputed using this randomly reduced spike train.

To measure the duration of post-trial, task-locked disruption of spatial information, we performed a rolling post-CS/US mutual-information analysis (Fig. S22). Beginning at CS/US offset, we

stepped through successive time windows and, for each window, removed only the calcium events within that window before recomputing spatial MI. For each window we also generated a spike-matched control distribution by removing an equal number of events selected randomly from the entire non-trial spike pool..

Computing bits per spike and bits per second

Bits per spike for spatial and trial periods was computed as follows[54]:

$$\text{bits per spike} = \sum_{i} \left(P_i \left(\frac{R_i}{R}\right) \log_2 \left(\frac{R_i}{R}\right) \right)$$

Where:

$i = spatial\ bin\ number$ or CSUS bin number

$P_i = occupancy\ probability\ for\ bin\ i$

$R_i = mean\ firing\ rate\ at\ bin\ i$

$R = overall\ mean\ firing\ rate$

Bits per second for spatial and trial periods was computed as follows[54]:

$$\text{bits per second} = \sum_{i} \left(P_i \, (R_i) \log_2 \left(\frac{R_i}{R}\right) \right)$$

Bits per spike and bits per second were computed for both spatial (non-trial) and trial epochs (0–2 s post-CS) using the same occupancy-normalized bin structure as the MI analysis. These measures identified a similar proportion of spatially and trial-modulated neurons, and trial-period bits-per-second values were positively associated with spatial bits-per-second across neurons.

Cross-epoch information comparisons

To determine whether spatial and trial-related information were correlated beyond shared firing-rate structure, we performed firing-rate–residualized comparisons (Fig. S4). For each neuron, we regressed spatial MI, trial-period MI, bits-per-spike, and bits-per-second against mean firing rate and computed residuals. Correlations were then computed between residual spatial and residual trial-period metrics. Residual MI and residual bits-per-spike remained significantly positively associated, indicating shared information beyond rate alone, whereas residual bits-per-second showed no consistent relationship.

Rate Map Masking and Task vs. Non-Task Firing Comparison

To assess whether calcium events during task periods occurred outside of typical place fields, we created spatial masks based on rate maps computed separately for task and non-task periods. First, task and non-task spike times were defined based on a 2-second window following each CS onset. We then

computed 2D firing rate maps using smoothed occupancy-normalized spatial histograms (bin size = 2.5 cm, event count and occupancy were each smoothed with a 2D gaussian kernel with σ = 0.5 bins) For each condition (task or non-task), we defined a binary spatial mask by thresholding the firing rate map at one standard deviations above the mean rate across bins. The non-task high-rate mask represents a putative place fields during each condition. Next, we computed the fraction of calcium events that occurred within each mask during both task and non-task periods. This yielded four firing rate values per neuron: task-period firing in task-defined mask, non-task-period firing in task-defined mask, task-period firing in non-task-defined mask, and non-task-period firing in non-task-defined mask. These values were compared using paired two-sided t-tests to assess whether activity in each spatial mask was significantly modulated by behavioral state.

To further quantify task-related changes in spatial firing, spatial masks were generated separately for task and non-task periods by thresholding occupancy-normalized rate maps at one standard deviation above the mean rate (Fig. S29). For each neuron we computed event rates within both masks during trial and non-trial periods. Comparisons of mask-restricted firing assessed whether task-period calcium events occurred preferentially in task-defined high-activity zones or non-task (place-field) zones.

Firing variability by location in place field and distance

For each animal and session, spatial place fields (PFs) were defined from non-task running (speed ≥ 4 cm/s; CS→CS+2 s excluded), using standard rate maps and thresholding contiguous regions with activity >1 SD above the mean. Task-related firing rates were computed on a trial-by-trial basis during the CS→2 s post-CS window.

To test whether spatial position influenced trial-to-trial variability of task-related firing, each trial was assigned an occupancy-mode centroid (highest-dwell spatial bin during the 0–2 s trial window). For each neuron, trial firing rates were compared between trials whose centroids fell inside versus outside the cell's non-trial place field (S26). Additional analyses examined the relationship between firing rate and centroid distance from the place-field center (Fig. S27) and the relationship between pairwise centroid proximity and pairwise firing-rate differences (Fig. S28). These analyses assessed whether place-field membership or spatial proximity modulated trial-period firing reliability.

To summarize position per trial, we used an occupancy-mode centroid: within the CS→2 s window we accumulated a 2-D histogram of the animal's x–y positions (bin size ≈2.5 cm) weighted by dwell time between samples, and selected the bin with maximal weighted occupancy; the bin center served as the trial's centroid. The histogram grid was aligned to the non-task rate-map grid so that centroid lookup into the PF mask was consistent. (This avoids arithmetic-mean centroids drifting into unvisited space, e.g., for perimeter trajectories.)

Each trial was then assigned both a firing rate (per cell) and a spatial centroid. For each cell, we formed all pairwise comparisons of task firing rates across trials. Pairs were categorized as “in-field” or “out-of-field” depending on whether both trials’ centroids fell within or outside the cell’s non-task-defined PF. We computed absolute and normalized differences in firing rate across trial pairs and compared in-field vs out-of-field variability using paired, two-sided t-tests.

In parallel, we examined the relationship between spatial proximity and variability irrespective of PF membership: pairwise Euclidean distances between trial centroids were regressed against firing-rate differences to obtain Pearson correlation coefficients (r) and p-values for each cell. At the population level, we pooled across cells and animals, and also aggregated results into rat-level summaries before pooling.

Spatial interference in task coding: population-vector (PV) and single cell analysis

For each recording day, calcium event activity was aligned to imaging frames and analyzed within a fixed cue-aligned trace window (CS to CS + 2 s). Animal position was discretized into a coarse two-dimensional spatial grid (2 × 2), and neural activity was converted to framewise per-cell event rates. Prior to downstream analyses, activity was centered around the mean across time so that similarity metrics reflected relative modulation patterns rather than global firing-rate differences. The trace window was subdivided into 15 equal temporal bins. For each trial, temporal bin, and spatial bin, a population vector (PV) was computed as the mean activity across cells for frames in the corresponding temporal–spatial intersection.

To quantify spatial structure during the trace task, PV similarity was assessed using a split-half procedure. Within each temporal bin and spatial bin, trials were randomly divided into two non-overlapping halves. Mean PV templates were computed separately for each half. SAME-space similarity was defined as the Pearson correlation between templates from the same spatial bin across halves, with DIFFERENT-space was the Pearson correlation between templates from different spatial bins across halves. Correlations were Fisher-z transformed and averaged across spatial bins and temporal bins to yield day-level similarity measures.

Split-half resampling was repeated 50 times per day, and results were averaged across resamples to obtain stable day-level estimates. Day-level values were then averaged across days within each animal. Statistical significance was assessed using paired comparisons in Fisher-z space at both the day level (n = 15 days) and the animal level (n = 5 rats). Values shown in figures are inverse Fisher-transformed (tanh) for interpretability.

For single-cell analyses, the same temporal and spatial binning and split-half procedure were used. For each neuron, temporal activity vectors across bins were computed separately for each spatial bin and split half. SAME-place correlations were defined as correlations between temporal vectors from the same spatial bin across halves, with OUT–OUT and IN–OUT controls defined analogously. Fisher-z–

transformed correlations were averaged across neurons to yield day-level and animal-level similarity measures.

Task interference in spatial coding: population-vector (PV) and single cell analysis

For each recording day, neural activity was aligned to imaging frames and assigned to a 2x2 spatial grid. “Control” (non-task) frames were defined by excluding all frames within a cue-aligned task window (CS:CS+2s) plus an optional post-window buffer; analyses optionally applied a running-speed threshold. Control frames were randomly split into two halves. For each spatial bin, population vectors (PVs) were computed as the mean per-cell activity across frames in that bin. Prior to constructing rate maps and population vectors, activity was centered around the mean per cell to remove cell-specific baseline rate offsets so that similarity metrics reflected relative spatial modulation patterns rather than global firing-rate differences (although results were consistent when not centered around the mean).

One half of the control data was used to construct a spatial template PV for each bin, and without-task spatial reliability was quantified as the Pearson correlation between the template PV and the PV computed from the held-out control half (split-half reliability).

To quantify spatial coding during the task, PVs were computed from frames within the task window and grouped by spatial bin. For each bin, the task PV was correlated with the corresponding control template PV from the same day. Correlations were Fisher-z transformed and averaged across bins to yield a day-level spatial similarity measure, which was then averaged across days within each animal (Fig. 4e).

For single-cell analyses (Fig. 4f), the same framework was applied at the level of individual neurons: spatial firing maps were constructed per cell across bins, and reliability was quantified as the correlation of each cell’s spatial map across conditions or split halves, followed by Fisher-z averaging across cells.

To reduce sampling variability, the control split and template construction were repeated 50 times with random resampling, and Fisher-z values were averaged across resamples prior to statistical testing. Task effects were assessed by comparing with-task versus without-task Fisher-z values using a within-day sign-flip permutation test applied to bin-wise differences, yielding two-sided p-values that preserve spatial structure while randomizing task labels. Values shown in figures reflect the inverse Fisher transform (tanh) of mean z values for interpretability.

For spatial stability analysis (Fig. 4g), for each animal and recording day, we quantified the stability of coarse spatial firing patterns on a fixed 2×2 spatial grid. To reduce across-cell rate offsets unrelated to spatial patterning, rate maps were optionally normalized per day by centering each cell around its mean using pooled finite map entries across all bins and windows, applied identically to task and non-task maps.

We estimated spatial stability using split-half correlations to reduce the influence of single-window noise. For each day and condition (task, non-task), windows were randomly split into two halves

and averaged within each half to form independent estimates of the spatial firing pattern; this procedure was repeated 50 times with different random splits. We report two complementary stability metrics, each computed as Pearson correlation followed by Fisher z-transform and averaging in z-space. Single-cell map stability (SC) was computed per cell as the correlation between its 4-bin mean rate vector from half A and half B, using pairwise-valid bins (minimum 2 valid bins), and then averaged across cells and split-half repetitions. Population-vector stability (PV) was computed within each spatial bin as the correlation across cells between the half-A and half-B population vectors for that bin, using pairwise-valid cells (minimum 10 valid cells), and then averaged across bins and repetitions. Pearson correlation coefficients were Fisher z-transformed prior to averaging and statistical testing. Values shown in figures reflect the inverse Fisher transform (tanh) of mean z values for interpretability. Task vs non-task differences were assessed with paired t-tests performed on Fisher z values either at the animal level (mean across days within each animal) or pooled across day pairs.

1018 **References**

1019 1 Penfield, W. & Milner, B. Memory deficit produced by bilateral lesions in the
1020 hippocampal zone. *A.M.A. archives of neurology and psychiatry* **79**, 475-497 (1958).
1021 2 Scoville, W. B. & Milner, B. Loss of recent memory after bilateral hippocampal lesions.
1022 *Journal of neurology, neurosurgery, and psychiatry* **20**, 11-21 (1957).
1023 3 O'Keefe, J. & Dostrovsky, J. The hippocampus as a spatial map. Preliminary evidence
1024 from unit activity in the freely-moving rat. *Brain Res* **34**, 171-175 (1971).
1025 4 O'Keefe, J. Place units in the hippocampus of the freely moving rat. *Exp Neurol* **51**, 78-
1026 109 (1976).
1027 5 Knierim, J. J. From the GPS to HM: Place cells, grid cells, and memory. *Hippocampus* **25**,
1028 719-725 (2015). https://doi.org:10.1002/hipo.22453
1029 6 O'Keefe, J. & Krupic, J. Do hippocampal pyramidal cells respond to nonspatial stimuli?
1030 *Physiol Rev* **101**, 1427-1456 (2021). https://doi.org:10.1152/physrev.00014.2020
1031 7 O'Keefe, J. Do hippocampal pyramidal cells signal non-spatial as well as spatial
1032 information? *Hippocampus* **9**, 352-364 (1999). https://doi.org:10.1002/(SICI)1098-
1033 1063(1999)9:4<352::AID-HIPO3>3.0.CO;2-1
1034 8 Williams, D. A., Frame, K. A. & LoLordo, V. M. Discrete signals for the unconditioned
1035 stimulus fail to overshadow contextual or temporal conditioning. *Journal of*
1036 *Experimental Psychology: Animal Behavior Processes* **18**, 41 (1992).
1037 9 Eichenbaum, H. & Fortin, N. J. Bridging the gap between brain and behavior: cognitive
1038 and neural mechanisms of episodic memory. *Journal of the experimental analysis of*
1039 *behavior* **84**, 619-629 (2005).
1040 10 Fortin, N. J. in *Learning and memory a comprehensive reference* (ed John H. Byrne) 385-
1041 417 (Academic,, London, 2008).
1042 11 Wallenstein, G. V., Hasselmo, M. E. & Eichenbaum, H. The hippocampus as an associator
1043 of discontiguous events. *Trends in neurosciences* **21**, 317-323 (1998).
1044 12 Mau, W. *et al.* The Same Hippocampal CA1 Population Simultaneously Codes Temporal
1045 Information over Multiple Timescales. *Current biology : CB* **28**, 1499-1508 e1494 (2018).
1046 https://doi.org:10.1016/j.cub.2018.03.051
1047 13 Crystal, J. D. Evaluating evidence from animal models of episodic memory. *J Exp Psychol*
1048 *Anim Learn Cogn* **47**, 337-356 (2021). https://doi.org:10.1037/xan0000294
1049 14 Berger, T. W., Rinaldi, P. C., Weisz, D. J. & Thompson, R. F. Single-unit analysis of
1050 different hippocampal cell types during classical conditioning of rabbit nictitating
1051 membrane response. *J Neurophysiol* **50**, 1197-1219 (1983).
1052 https://doi.org:10.1152/jn.1983.50.5.1197
1053 15 McEchron, M. D. & Disterhoft, J. F. Sequence of single neuron changes in CA1
1054 hippocampus of rabbits during acquisition of trace eyeblink conditioned responses. *J*
1055 *Neurophysiol* **78**, 1030-1044 (1997). https://doi.org:10.1152/jn.1997.78.2.1030
1056 16 Wilmot, J. H., Puhger, K. & Wiltgen, B. J. Acute Disruption of the Dorsal Hippocampus
1057 Impairs the Encoding and Retrieval of Trace Fear Memories. *Front Behav Neurosci* **13**,
1058 116 (2019). https://doi.org:10.3389/fnbeh.2019.00116
1059 17 Wirtshafter, H. S., Solla, S. A. & Disterhoft, J. F. A universal hippocampal memory code
1060 across animals and environments. *bioRxiv*, 2024.2010.2024.620127 (2024).
1061 https://doi.org:10.1101/2024.10.24.620127
1062 18 Woodruff-Pak, D. S. & Disterhoft, J. F. Where is the trace in trace conditioning? *Trends*
1063 *Neurosci* **31**, 105-112 (2008). https://doi.org:10.1016/j.tins.2007.11.006
1064 19 Zuniga, A. *et al.* Extinction training suppresses activity of fear memory ensembles across
1065 the hippocampus and alters transcriptomes of fear-encoding cells.

Neuropsychopharmacology : official publication of the American College of Neuropsychopharmacology (2024). https://doi.org:10.1038/s41386-024-01897-0

20 Gauthier, J. L. & Tank, D. W. A Dedicated Population for Reward Coding in the Hippocampus. *Neuron* **99**, 179-193 e177 (2018). https://doi.org:10.1016/j.neuron.2018.06.008

21 Meshulam, L., Gauthier, J. L., Brody, C. D., Tank, D. W. & Bialek, W. Collective Behavior of Place and Non-place Neurons in the Hippocampal Network. *Neuron* **96**, 1178-1191 e1174 (2017). https://doi.org:10.1016/j.neuron.2017.10.027

22 Panoz-Brown, D. *et al.* Replay of Episodic Memories in the Rat. *Curr Biol* **28**, 1628-1634 e1627 (2018). https://doi.org:10.1016/j.cub.2018.04.006

23 Sheridan, C. L. *et al.* Replay of incidentally encoded episodic memories in the rat. *Current biology : CB* **34**, 641-647 e645 (2024). https://doi.org:10.1016/j.cub.2023.12.043

24 Allen, T. A., Salz, D. M., McKenzie, S. & Fortin, N. J. Nonspatial Sequence Coding in CA1 Neurons. *J Neurosci* **36**, 1547-1563 (2016). https://doi.org:10.1523/JNEUROSCI.2874-15.2016

25 Shahbaba, B. *et al.* Hippocampal ensembles represent sequential relationships among an extended sequence of nonspatial events. *Nat Commun* **13**, 787 (2022). https://doi.org:10.1038/s41467-022-28057-6

26 Ng, C. W., Elias, G. A., Asem, J. S. A., Allen, T. A. & Fortin, N. J. Nonspatial sequence coding varies along the CA1 transverse axis. *Behav Brain Res* **354**, 39-47 (2018). https://doi.org:10.1016/j.bbr.2017.10.015

27 Dong, S. *et al.* Decoding memory features from hippocampal spiking activities using sparse classification models. *Annu Int Conf IEEE Eng Med Biol Soc* **2016**, 1620-1623 (2016). https://doi.org:10.1109/EMBC.2016.7591023

28 Deadwyler, S. A., Berger, T. W., Opris, I., Song, D. & Hampson, R. E. Neurons and networks organizing and sequencing memories. *Brain Res* **1621**, 335-344 (2015). https://doi.org:10.1016/j.brainres.2014.12.037

29 Moyer, J. R., Jr., Deyo, R. A. & Disterhoft, J. F. Hippocampectomy disrupts trace eye-blink conditioning in rabbits. *Behav Neurosci* **104**, 243-252 (1990).

30 McEchron, M. D. & Disterhoft, J. F. Hippocampal encoding of non-spatial trace conditioning. *Hippocampus* **9**, 385-396 (1999). https://doi.org:10.1002/(SICI)1098-1063(1999)9:4<385::AID-HIPO5>3.0.CO;2-K

31 Weiss, C. *et al.* Trace eyeblink conditioning in the freely moving rat: optimizing the conditioning parameters. *Behav Neurosci* **113**, 1100-1105 (1999). https://doi.org:10.1037//0735-7044.113.5.1100

32 Thompson, R. F. The neurobiology of learning and memory. *Science* **233**, 941-947 (1986).

33 Berger, T. W., Alger, B. & Thompson, R. F. Neuronal substrate of classical conditioning in the hippocampus. *Science* **192**, 483-485 (1976).

34 Weiss, C. & Disterhoft, J. F. The impact of hippocampal lesions on trace-eyeblink conditioning and forebrain-cerebellar interactions. *Behav Neurosci* **129**, 512-522 (2015). https://doi.org:10.1037/bne0000061

35 Larra, M. F., Behrje, A., Finke, J. B., Blumenthal, T. D. & Schachinger, H. Filling the gap: Evidence for a spatial differentiation in trace eyeblink conditioning. *Neurosci Lett* **654**, 33-37 (2017). https://doi.org:10.1016/j.neulet.2017.06.011

36 Kehoe, E. J. Repeated acquisitions and extinctions in classical conditioning of the rabbit nictitating membrane response. *Learn Mem* **13**, 366-375 (2006). https://doi.org:10.1101/lm.169306

37 Shan, K. Q., Lubenov, E. V., Papadopoulou, M. & Siapas, A. G. Spatial tuning and brain state account for dorsal hippocampal CA1 activity in a non-spatial learning task. *eLife* **5** (2016). https://doi.org:10.7554/eLife.14321

38 Moita, M. A., Rosis, S., Zhou, Y., LeDoux, J. E. & Blair, H. T. Hippocampal place cells acquire location-specific responses to the conditioned stimulus during auditory fear conditioning. *Neuron* **37**, 485-497 (2003). https://doi.org:10.1016/s0896-6273(03)00033-3

39 MacDonald, C. J., Carrow, S., Place, R. & Eichenbaum, H. Distinct hippocampal time cell sequences represent odor memories in immobilized rats. *J Neurosci* **33**, 14607-14616 (2013). https://doi.org:10.1523/JNEUROSCI.1537-13.2013

40 Moser, E. I., Moser, M.-B. & McNaughton, B. L. Spatial representation in the hippocampal formation: a history. *Nature neuroscience* **20**, 1448-1464 (2017).

41 Skaggs, W. E., McNaughton, B. L., Wilson, M. A. & Barnes, C. A. Theta phase precession in hippocampal neuronal populations and the compression of temporal sequences. *Hippocampus* **6**, 149-172 (1996). https://doi.org:10.1002/(SICI)1098-1063(1996)6:2<149::AID-HIPO6>3.0.CO;2-K

42 Wirtshafter, H. S. & Disterhoft, J. F. Place cells are nonrandomly clustered by field location in CA1 hippocampus. *Hippocampus* **33**, 65-84 (2023). https://doi.org:10.1002/hipo.23489

43 Wirtshafter, H. S. & Disterhoft, J. F. In Vivo Multi-Day Calcium Imaging of CA1 Hippocampus in Freely Moving Rats Reveals a High Preponderance of Place Cells with Consistent Place Fields. *J Neurosci* (2022). https://doi.org:doi: 10.1523/JNEUROSCI.1750-21.2022

44 Weiss, C. & Thompson, R. F. The effects of age on eyeblink conditioning in the freely moving Fischer-344 rat. *Neurobiol Aging* **12**, 249-254 (1991). https://doi.org:10.1016/0197-4580(91)90105-s

45 Skelton, R. W. Bilateral cerebellar lesions disrupt conditioned eyelid responses in unrestrained rats. *Behav Neurosci* **102**, 586-590 (1988). https://doi.org:10.1037//0735-7044.102.4.586

46 Aharoni, D., Khakh, B. S., Silva, A. J. & Golshani, P. All the light that we can see: a new era in miniaturized microscopy. *Nat Methods* **16**, 11-13 (2019). https://doi.org:10.1038/s41592-018-0266-x

47 Silva, A. J. Miniaturized two-photon microscope: seeing clearer and deeper into the brain. *Light: Science & Applications* **6**, e17104-e17104 (2017).

48 Mathis, A. *et al.* DeepLabCut: markerless pose estimation of user-defined body parts with deep learning. *Nature neuroscience* **21**, 1281-1289 (2018).

49 Corder, G. *et al.* An amygdalar neural ensemble that encodes the unpleasantness of pain. *Science* **363**, 276-281 (2019). https://doi.org:10.1126/science.aap8586

50 Thevenaz, P., Ruttimann, U. E. & Unser, M. A pyramid approach to subpixel registration based on intensity. *IEEE Trans Image Process* **7**, 27-41 (1998). https://doi.org:10.1109/83.650848

51 Zhou, P. *et al.* Efficient and accurate extraction of in vivo calcium signals from microendoscopic video data. *eLife* **7** (2018). https://doi.org:10.7554/eLife.28728

52 Kinsky, N. R., Sullivan, D. W., Mau, W., Hasselmo, M. E. & Eichenbaum, H. B. Hippocampal Place Fields Maintain a Coherent and Flexible Map across Long Timescales. *Current biology : CB* **28**, 3578-3588 e3576 (2018). https://doi.org:10.1016/j.cub.2018.09.037

53 Olypher, A. V., Lansky, P., Muller, R. U. & Fenton, A. A. Quantifying location-specific information in the discharge of rat hippocampal place cells. *J Neurosci Methods* **127**, 123-135 (2003). https://doi.org:10.1016/s0165-0270(03)00123-7

54 Wirtshafter, H. S. & Wilson, M. A. Differences in reward biased spatial representations in the lateral septum and hippocampus. *eLife* **9** (2020). https://doi.org:10.7554/eLife.55252

Acknowledgements: This work was supported by an NIA T32 (T32-AG020506/AG/NIA), an NIA R37 (R37-AG008796/AG/NIA), an NINDS R01 (R01 NS113804/NS/NINDS), and a K99 award (K99 MH135062). We would like to thank all members of the Disterhoft lab, especially Mackenzie Kneisly.

Author contributions: Investigation, H.S.W.; Formal Analysis, H.S.W.; Writing – Original Draft, H.S.W.; Writing – Review & Editing, H.S.W., M.R.M, S.A.S., J.F.D.; Funding: H.S.W, J.F.D., Supervision, M.R.M, S.A.S., J.F.D.

Declaration of interests: The authors declare no competing interests.